Microstructural evolution during film growth

I. Petrov[a)]
Frederick Seitz Materials Research Laboratory and Department of Materials Science, University of Illinois, Urbana, Illinois 61801

P. B. Barna
Research Institute for Technical Physics and Materials Science, Hungarian Academy of Sciences, Budapest H-1325, Hungary

L. Hultman
Thin Film Division, Physics Department, Linköping University, S-581 83 Linköping, Sweden

J. E. Greene
Frederick Seitz Materials Research Laboratory and Department of Materials Science, University of Illinois, Urbana, Illinois 61801

Atomic-scale control and manipulation of the microstructure of polycrystalline thin films during kinetically limited low-temperature deposition, crucial for a broad range of industrial applications, has been a leading goal of materials science during the past decades. Here, we review the present understanding of film growth processes—nucleation, coalescence, competitive grain growth, and recrystallization—and their role in microstructural evolution as a function of deposition variables including temperature, the presence of reactive species, and the use of low-energy ion irradiation during growth. © *2003 American Vacuum Society.* [DOI: 10.1116/1.1601610]

I. INTRODUCTION

Polycrystalline thin films have found diverse applications ranging from metallization and dielectric layers to optical, magnetic, and tribological coatings, to diffusion and thermal barriers. Progress in thin film science and technology accelerated following the maturation of vacuum technology which gave birth to the American Vacuum Society (AVS) in 1953. The first divisions within the AVS, the Vacuum Metallurgy Division (today the Advanced Surface Engineering Division) and the Thin Film Division both focused on polycrystalline coatings and thin films. In subsequent years, understanding of thin film synthesis has benefited tremendously from advances in the areas of surface science and analysis.

Thin films exhibit a wide variety of microstructures characterized in terms of grain size and crystallographic orientation, lattice defects, phase composition, and surface morphology. Industrial demand for ever lower processing temperatures in device and product manufacturing means that films are often deposited at temperatures T_s which are less that 0.2–0.3 of the melting point T_m (in degrees K). Thus, film synthesis generally takes place far from thermodynamic equilibrium. As a consequence, microstructure during deposition typically evolves in a competitive fashion and the kinetic limitations induced by low-temperature growth allow for the controlled synthesis of metastable phases and artificial structures such as multilayers and nanophase materials.

Among the determinant atomic processes controlling structure evolution during film deposition are surface and bulk diffusion. These processes are affected by, in addition to T_s, energetic particle bombardment which can be used to manipulate adatom mobilities and nucleation rates. The presence of alloying or impurity elements and their segregation to surfaces and grain boundaries can also strongly influence the final result.

Extensive studies of the correlation between film structure and deposition parameters have been carried out over the past five decades. From an understanding of film formation, follows the possibility for microstructural and nanostructural engineering in order to design a material for specific technological applications. This has led to the development and refinement of structure zone models (SZMs) which systematically categorize self-organized structural evolution during physical vapor deposition (PVD) as a function of film growth parameters.[1–7] The history of SZMs has been reviewed by Thornton[8] and Barna and Adamik.[9] In 1969, Movchan and Demchishin[1] observed that the microstructural evolution of evaporated Ti, Ni, W, ZrO_2, and Al_2O_3 coatings can be systematically represented by a single SZM diagram plotted versus film thickness and the homologous temperature T_s/T_m. Significant contributions to the understanding of microstructural evolution in PVD thin films are documented in Refs. 10–37. Electro-deposition and chemical vapor deposition, representing extreme cases of low- and high-temperature growth regimes, exhibit many features of microstructural evolution which are analogous to PVD due to similarities in the atomistics of the growth processes.[38]

The first SZMs were derived from relatively low-resolution optical and scanning electron microscopy observations. Later, cross-sectional transmission electron microscopy (XTEM) and scanning probe microscopy (SPM) analyses were employed to provide more detailed structural characterization. *In situ* electron microscopy has revealed the

---

[a)]Author to whom correspondence should be addressed; electronic mail: petrov@uiuc.edu

dynamics of film growth. This, together with results from *in situ* SPM studies and computational materials science, has provided detailed atomistic insights into microstructural evolution during polycrystalline film growth.

This article is a short review of recent progress in understanding microstructural evolution in thin films synthesized by low-temperature PVD on amorphous and polycrystalline substrates. The use of amorphous substrates allows the experimentalist to isolate the effects of individual deposition variables on texture development. Polycrystalline substrates bias texture through local pseudomorphic epitaxy, however the overall microstructure will still evolve toward a final state driven by the extant deposition conditions. On both types of substrates, film growth proceeds via a three-dimensional (3D) or Volmer–Weber mode. Related areas of thin film science and technology not treated here are modeling of nucleation kinetics (see companion article by Ratsch and Venables[39] in this volume), epitaxial layer formation, and surface morphological evolution during epitaxy (article by Cahill[40] in this volume).

We begin in Sec. II by introducing the fundamental film growth processes, and resulting SZMs, for PVD synthesis of pure elemental films. Then we describe SZMs for reactive deposition of multicomponent systems and discuss the effects of dopant and alloying elements (whether intentional or not), as well as phase formation, on the resultant nano- and microstructures (Sec. III). In Sec. IV, we describe the effects of ion irradiation in modifying film structure during deposition.

II. GROWTH OF PURE ELEMENTAL POLYCRYSTALLINE FILMS

The growth processes controlling microstructural evolution, presented schematically in Fig. 1, include nucleation, island growth, impingement and coalescence of islands, formation of polycrystalline islands and channels, development of a continuous structure, and film growth. When surface diffusion rates are significant, film thickening proceeds through local epitaxy on individual grains. Grain coarsening, i.e., recrystallization through grain boundary (GB) migration, can occur both during and after island coalescence.

The nucleation barrier is generally expected to be small, leading to randomly oriented islands, for low-temperature deposition on amorphous substrates.[31,36] *In situ* TEM investigations confirm this for studies of Au/SiO$_2$[41] and In/C.[42] In the latter case, nucleation of In deposited on amorphous C substrates at $T_s/T_m < 0.4-0.5$ results in solid-phase islands with random orientation, while at higher temperature the nuclei are liquid due to the suppressed melting point of nanoscale particles.[43] Nucleation kinetics is affected by the adatom binding energy, crystal structure of the substrate material, lattice defects, surface steps, and contamination.

During island coalescence, there is a strong driving force for coarsening through surface atom diffusion and GB motion. The island with lower energy per atom consumes the other(s), resulting in a new single-crystal island as the system attempts to minimize the overall surface and interface
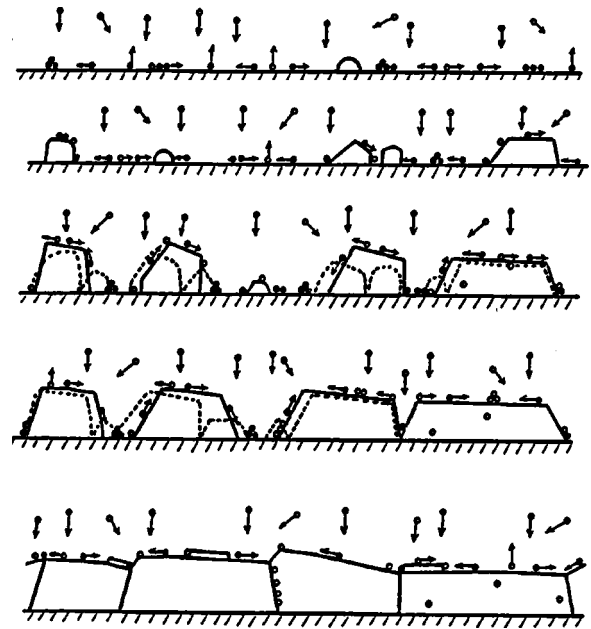

FIG. 1. Schematic diagram illustrating fundamental growth processes controlling microstructural evolution: nucleation, island growth, impingement and coalescence of islands, grain coarsening, formation of polycrystalline islands and channels, development of a continuous structure, and film growth (see Ref. 9).

energy. Thus, coarsening during coalescence is the first and most active phenomenon leading to selection of preferred orientation.[44] Islands with the densest planes are typically selected; that is, (111) for fcc, (0002) for hcp, and (110) for bcc. Depending on temperature and island size, coarsening can be very fast, often termed liquid-like coalescence, occurring by either rapid surface diffusion or by melting (for low melting-point materials) upon contact followed by crystallization. The driving force is the release of edge and surface energy associated with island coalescence. Rapid coalescence also results in new open substrate area for secondary nucleation. At lower temperatures or larger island sizes, coarsening is slower and proceeds through GB migration. Grain coarsening during coalescence of the contacting crystals is repeated until the local grain size becomes sufficiently large that grain boundaries are immobile. Figure 2 illustrates several coarsening events during coalescence of In islands on amorphous C.[45]

The SZM in Fig. 3, characterizing microstructure evolution in pure elemental films, consists of three regions:[9] Zone I corresponds to very low deposition temperatures at which adatom diffusion is negligible; surface diffusion becomes significant in the transition Zone T; and Zone II represents film growth at deposition temperatures for which both surface and bulk diffusion are operative. The boundaries between the zones are diffuse and "transitions" occur gradually over wide ranges in T_s/T_m.

During film growth in the low-T_s Zone I regime (Fig. 3), an underdense structure with a fine fiber texture develops. Initial in-plane grain sizes are set by the saturation nucleation density. Adatom mobilities are low and columns preserve the random orientation of the nuclei as predicted by ballistic
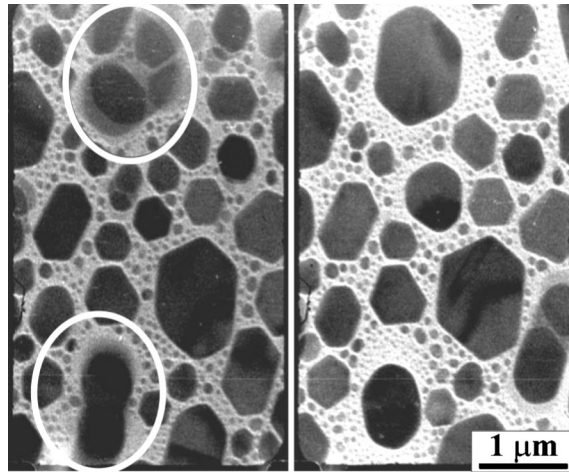
FIG. 2. *In situ* plan-view TEM micrographs obtained during the growth and coalescence of In islands deposited at 0.5 nm s^{-1} on amorphous C substrates at $T_s = 40\,°C$. The time lapse between obtaining the left and right images is 0.3 s. Note the denuded zones surrounding the coalesced islands (see Ref. 45).

FIG. 4. Kinetic Monte Carlo simulation of competitive texture evolution during low-temperature sputter deposition of an Al film. Islands (and later columns) with lighter contrast are 001 oriented, while darker islands/ columns are 111 oriented (see Ref. 48).

models.[15,46] The columns are generally not single grains, but are composed of smaller more equiaxed grains, or can be completely amorphous. Surface roughness develops in a fractal geometry[47] which, due to wide angular distribution of the deposition flux, atomic shadowing, and limited surface diffusion, leads to extensive porosity.

At higher film growth temperatures (Zone T), grain coarsening occurs during coalescence of small islands with large surface to volume ratios, while grain boundaries become immobile in continuous films. Orientation selection during coarsening is incomplete, thus crystallites are nearly random or only weakly textured and there is a wide distribution of grain sizes. The orientation and size of individual crystallites will determine their behavior during subsequent growth processes characterized by the competition among neighboring
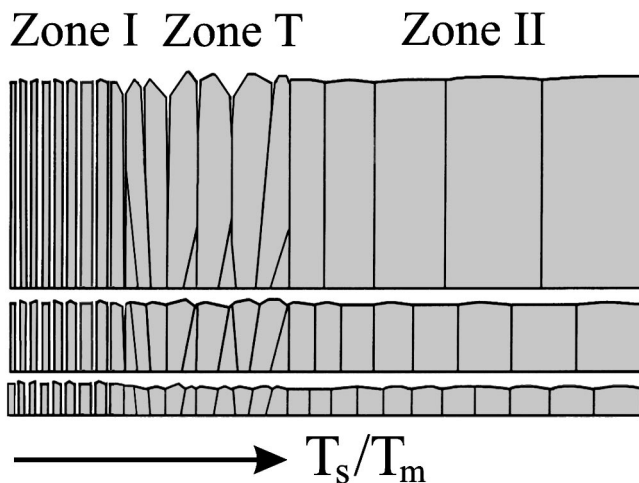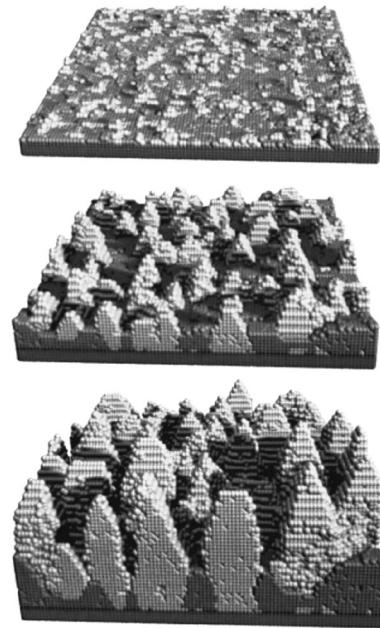

FIG. 3. SZM schematically representing microstructural evolution of pure elemental films as a function of the reduced temperature T_s/T_m, where T_s is the deposition temperature and T_m is the melting point of the material, both expressed in degrees K (see Ref. 9).

grains. In this T_s/T_m range, adatom surface diffusion is significant resulting in local epitaxial growth taking place on individual grains. Pronounced columnar structure develops in which the columns are actually elongated grains.

The primary features of Zone T competitive grain growth are illustrated by the kinetic Monte Carlo (kMC) simulation of Gilmer *et al.*[48] (Fig. 4) for Al growth. While there are initially equal distributions of 111 and 001 islands, the latter orientation eventually dominates due to anisotropies in surface diffusivities and adatom potential energies. That is, the average adatom residence time is significantly higher at lattice sites on low diffusivity (low potential energy) 001 surfaces versus high diffusivity (high potential energy) 111 surfaces. Thus, adatoms which are stochastically deposited near grain boundaries and, through surface diffusion, sample sites on both sides of the boundary have a higher probability of becoming incorporated at the low-diffusivity surface which provides the more stable, lower potential energy sites. Conversely, adatoms on high diffusivity planes have longer mean free paths with correspondingly higher probabilities to move off the plane and become trapped on adjacent grains. Thus, 001 grains with low surface diffusivities grow faster. Atomic shadowing exacerbates the difference, as protruding surfaces capture more off-normal flux. Thus, low-diffusivity 001 grains slowly expand, overgrow the high-diffusivity grains, and become bounded by 111 facets. This leads to considerable surface roughness which scales with the average in-plane grain size.

The consequence of competitive growth is a continuous change in morphology, texture, and surface topography (and, hence, film properties!) as a function of film thickness. Near the substrate, the microstructure consists of randomly ori-

ented small grains out of which V-shaped columns with the favored orientations slowly emerge and overgrow kinetically disadvantaged columns. This gives rise to increased preferred orientation. The faceted column tops result, as noted above, in surface roughness which increases with thickness giving rise to open column boundaries due to atomic shadowing.

At still higher T_s/T_m (Zone II), bulk diffusion becomes significant. GB migration takes place not only during coalescence, but throughout the film thickening process. Orientation selection during the coalescence stage is more pronounced and is driven by a decrease in the total GB area as well as minimization of interface and surface energy.[35] Large grains with low surface and interface energy grow at the expense of smaller or unfavorably oriented grains. Normal grain growth is impeded if the grains have a strong texture, i.e., if the orientation selection was completed during coalescence, or the mean in-plane grain diameter reaches two to three times the film thickness.[35] Secondary recrystallization, also called abnormal grain growth, may follow in which the grain size distribution is transformed from monomodal, through bimodal, to a new monomodal distribution with much larger in-plane grain size. During secondary recrystallization, the degree of texture is further enhanced. The film structure is homogenous in the growth direction and composed of columnar crystals with flat surfaces decorated by GB grooves.

III. REACTIVE DEPOSITION PROCESSES: GROWTH OF MULTICOMPONENT AND/OR MULTIPHASE FILMS

Possibilities for controlling structural evolution during growth of pure elemental films are limited and the structures obtained are unstable against temperature increases. Thus, during use the layers tend to restructure toward thermodynamic equilibrium. The effects of additives (contaminants, dopants, or alloying elements) in controlling the grain size are well known in bulk materials. Similarly, polycrystalline thin films synthesized by reactive deposition provide additional pathways for microstructure control while yielding enhanced thermal and process stability. It is important to note that even very low concentrations (sometimes below the detection limits of modern analytical techniques) of unintentionally incorporated atmospheric contaminants such as water vapor,[49] oxygen, and hydrocarbons, may be active as "grain refiners."[50]

Consider the case of O-containing Al films deposited at room temperature, a T_s value which corresponds to Zone II in the pure-Al SZM.[51] Observed changes in film structure and orientation as a function of increasing oxygen concentration are summarized in Fig. 5.[9] Oxygen has low solubility in Al and segregates to surfaces and grain boundaries where it forms two-dimensional (2D) oxide layers (oxide tissue phases) which greatly reduce Al surface and GB mobilities. These layers modify all thin film formation processes, limiting grain coarsening during coalescence and film growth. They also periodically interrupt the epitaxial growth of indi-
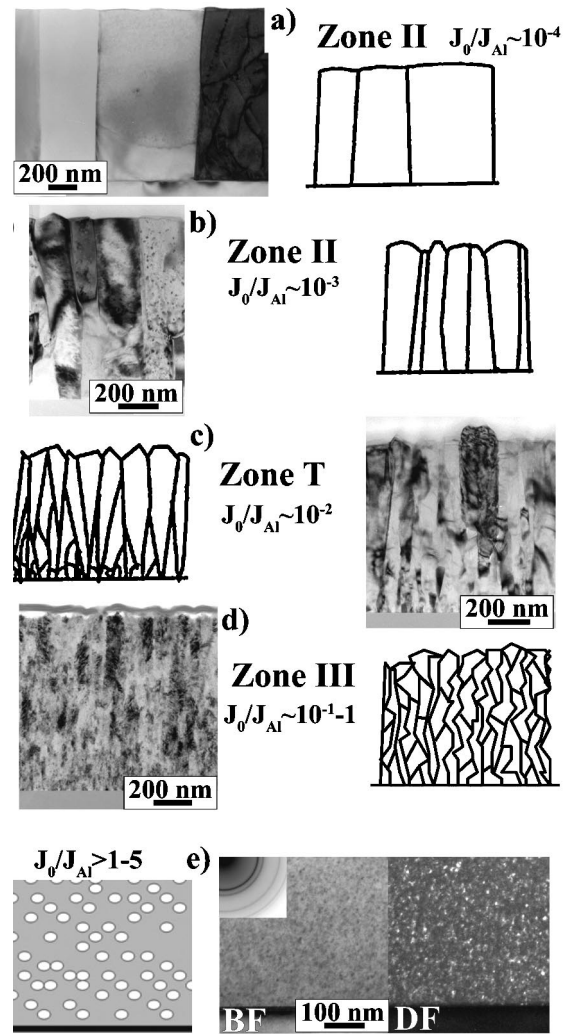

FIG. 5. XTEM images with corresponding schematic diagrams showing the microstructure of Al films deposited by thermal evaporation on amorphous SiO$_2$ at room temperature as a function of the incident O to Al flux ratio J_O/J_{Al} (see Ref. 9).

vidual crystallites and cause renucleation.[42] By exploiting these phenomena, new micro- and nanostructures can be controllably formed.[9]

At low O/Al arrival rate ratios, $J_O/J_{Al} \sim 10^{-3}$, oxygen is incorporated into the grain boundaries and continues to accumulate during GB migration, eventually inhibiting grain coarsening through "impurity drag." The resulting texture remains Zone II with columns extending through the film, but with a lesser degree of preferred orientation and a smaller grain size as shown in Fig. 5(b).

With slightly higher oxygen concentration levels ($J_O/J_{Al} \sim 10^{-2}$), coarsening during coalescence is severely suppressed, resulting in grains with random orientation. The competitive growth which follows is governed by anisotropic crystallographic effects[52] (O segregates fastest at 111 surfaces). Oxygen is incorporated into the lattice of 001 and 110 crystal faces, while an oxide layer is formed on the 111 faces.[53] The oxide layer forms as oxygen tends to accumulate at step edges on 111 surfaces, blocking step motion and

forming step bunches. These pinning sites serve to nucleate the oxide phase. Neighboring 111 grains form rounded edges due to oxygen segregation while 111-oriented grains in contact with 001 facets remain sharp, as oxygen is incorporated in the latter. The 111 grains eventually develop rounded surfaces indicating that local epitaxial Al growth has been interrupted by an oxide layer, above which renucleation of metal islands takes place. Crystal growth on 001-oriented grains is unimpeded by oxygen; these grains protrude above the average film surface and eventually win in competitive growth. They develop the shape of truncated octahedrons bounded by a 001 top face and 111 side faces. The degree of 001 preferred orientation increases with film thickness and is accompanied by greater surface roughness with increasing oxygen concentrations [Fig. 5(c)].

At still higher oxygen concentrations ($J_O/J_{Al} \sim 0.1-1$), the oxide layer completely covers islands of all orientations at an early stage and coarsening during coalescence is blocked. Thus, film growth proceeds by repeated renucleation. The film is composed of 3D equiaxed (globular) grains with random orientation and the Zone III structure [Fig. 5(d)] introduced in Ref. 1. With increasing oxygen concentration, the grain size decreases and can reach the nanometer range. An important byproduct of repeated nucleation for nanograin film formation is that surface faceting on individual columns, and the related shadowing effects, are eliminated. Thus, nanophase films are inherently much smoother, and as a result, denser. The presence of oxide phases also inhibits GB migration in the bulk of the film, preventing grain coarsening and imparting higher thermal stability.

O/Al has been used as a model system for investigating the growth of nanocrystalline (nc) grains separated by an amorphous tissue phase (a-AlO$_x$ in this case), as indicated in Fig. 5(d), through continuous segregation and renucleation processes. This technique has been systematically exploited in order to synthesize "superhard" nanocomposite films based on transition metal (TM) nitrides and carbides, e.g., nc-TMN/a-Si$_3$N$_4$,[54] nc-TMC/a-C,[55]   TiN$_x$B$_y$ and TiC$_x$B$_y$,[56] TMN/Cu,[57] and YSZ/Au.[58]

As the oxygen concentration is further increased, ($J_O/J_{Al} \sim 2-5$), the role of the oxide and metal phases is reversed: the oxide phase nucleates first while Al segregates to the surface and forms 3D islands.[51,59] Resulting films are composed of metallic grains dispersed in an oxide matrix [Fig. 5(e)].[60] Such composite films, consisting of a low-diffusivity matrix with higher-diffusivity metallic inclusions, are the basis of a class of ceramic-metallic coatings with diverse applications: resistors,[61] sensors,[62] solar cell elements,[63] low-friction hard coatings (e.g., TM/a-C[64]), and tribological coatings that adapt to the environment.[65]

At very high oxygen fluxes ($J_O/J_{Al} \gg 1$), the films consist entirely of aluminum oxide, which for room temperature growth is amorphous. T_s values exceeding 800 °C are required for the synthesis of the chemically and mechanically stable κ and α crystalline phases of alumina. There has, however, been a concerted effort to achieve hard crystalline alu-
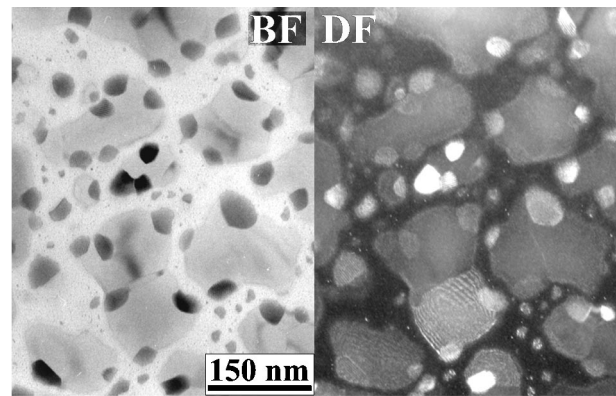

FIG. 6. Bright-field (BF) and dark field (DF) TEM images of a 35-nm-thick Al+4 at. % Pt layer co-evaporated on amorphous C at $T_s = 350$ °C. The DF image was obtained using Al$_5$Pt and Al$_6$Pt diffraction rings (see Ref. 68).

mina using ion irradiation during growth at temperatures below 500 °C.[66]

Figures 6 and 7 illustrate two more examples of microstructural evolution in multi-component films. Both of these cases involve only metallic elements. Figure 6 is a plan-view TEM image of a 35-nm-thick Al+4 at. % Pt film, deposited at $T_s = 350$ °C. Phase identification by electron diffraction and dark field imaging[67] shows that the larger grains with brighter contrast are fcc Al while the smaller and darker grains are a mixture of Al$_5$Pt and Al$_6$Pt. In contradistinction to the 2D "tissue phases" formed in the Al/O system, the adspecies composing all three phases in this system have high surface mobilities and the minority phases (Al$_5$Pt and Al$_6$Pt) nucleate 3D islands on the surface of the majority phase. Equiaxed grains of the minority phase decorate grain boundaries and triple points, thus significantly decreasing GB migration and grain coarsening.[68] This type of microstructural evolution has been observed in the Al(Cu) system used for metallization in microelectronic circuits.[37]

The addition of Sn to Al has quite the opposite effect; rather than to decrease the grain size as O and Pt described above, it acts as a grain size promoter.[9] The plan-view TEM image in Fig. 7, from a co-evaporated Al–Sn film with an in-plane compositional gradient, reveals a continuous in-
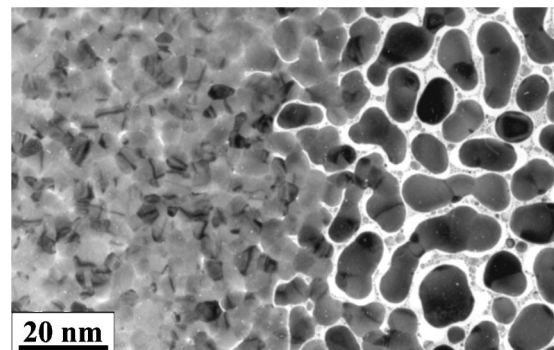

FIG. 7. Bright-field plan-view TEM micrograph of a 100-nm-thick Al–Sn film deposited on amorphous C at room temperature. The Sn concentration varies from 0 at the left edge of the image to 10 at. % at the right edge (see Ref. 69).

crease in grain size from left to right. The Sn concentration varies from 0 at the left edge of the micrograph to ~10 at. % at the right edge. At low Sn concentrations, the film is continuous with an average grain size of 3–5 nm, while at higher concentrations the film is still in the island growth stage with the grain size enhanced by a factor of >5. Sn appears to be acting as a surfactant in increasing the Al surface mobility.[69]

IV. EFFECTS OF ION IRRADIATION ON MICROSTRUCTURE AND TEXTURE EVOLUTION

Low-energy ion irradiation during growth is used extensively to overcome the characteristically rough and underdense microstructures (Zones I and T) of refractory materials deposited at low T_s (typically $T_s/T_m < 0.25$).[18–20,25,70] Under the correct set of deposition conditions, ion bombardment has been shown to increase nucleation rates and film density, to decrease average grain size, to inhibit the formation of columnar structures associated with high surface roughness, and to controllably affect the defect density and orientation of coatings. Because of their technological importance, TiN and related TM nitrides have served as model systems to study ion-assisted growth and we will use them as examples to illustrate the roles of ion flux and ion energy on microstructure evolution. For ease of discussion, we separate ion-irradiation effects into three regimes characterized by the ratio of the ion to metal J_i/J_{Me} fluxes incident at the growing film surface and the average ion energy E_i: (i) $J_i/J_{Me} \leq 1$ with $E_i \leq 20$ eV, (ii) $J_i/J_{Me} \leq 1$ with $E_i \geq 100$ eV, and (iii) $J_i/J_{Me} \geq 5$ with $E_i \leq 20$ eV.

A. Low-temperature film growth with low-energy, low-flux ion irradiation

In this section, we consider microstructural evolution of TiN and $Ti_{0.5}Al_{0.5}N$ films deposited on SiO_2 or steel substrates by reactive sputtering in Ar + N_2 mixtures. The N_2 fraction in the sputtering gas mixture corresponds to several percent and is optimized to obtain stoichiometric films while maximizing the deposition rate by maintaining a nonpoisoned target surface. Under such conditions, the dominant ion incident at the growing film is Ar^+ with energy corresponding approximately to the applied negative substrate bias V_s.[71] That is, $E_i = e(V_s - V_{pl}) \approx eV_s$, where V_{pl} is the plasma potential which is close to that of the grounded anode under typical magnetron sputtering conditions.

Figure 8 is a XTEM image illustrating the extremely open microstructure (Zone I) of TM nitrides deposited at low T_s. The micrograph is from the top portion of a 3-μm-thick TiN film grown at $T_s = 500$ °C, with $J_i/J_{Ti} = 0.5$, $E_i = 100$ eV, and a total pressure P_t of 38 mTorr.[72] P_t is approximately an order of magnitude higher than typical values used in magnetron sputtering in order to thermalize the energetic particle fluxes (sputtered and reflected) from the target. The thermalization distance d_{th} of sputtered and reflected species is approximately a factor of 5 smaller that the target substrate separation d_{ts}.[73] Despite the relatively high ion energy, the microstructure is columnar and very porous with both inter-
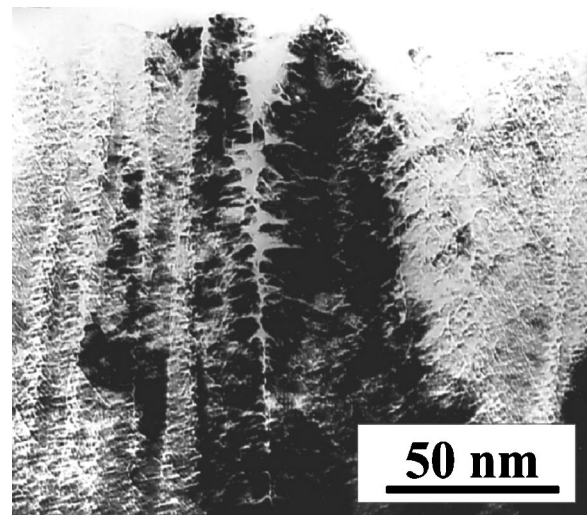

FIG. 8. Bright-field XTEM micrograph obtained from the top portion of a 3-μm-thick TiN film deposited on steel at 500 °C with a total pressure $P_t = 38$ mTorr. The ion-to-Ti flux ratio J_i/J_{Ti} incident at the film surface was 0.5 with an ion energy $E_i = 100$ eV.

and intra-columnar voids outlining a pronounced dendritic pattern. Such an open structure is due to limited surface diffusion.

Magnetron sputter deposition is generally carried out at pressures for which $d_{ts} < d_{th}$. The deposited flux is thus hyperthermal (average sputtered atom energies are ~10 eV with a high-energy tail extending to >100 eV), resulting in Zone T microstructures. Figure 9 is a XTEM micrograph of a TiN film grown on amorphous SiO_2 at $P_t = 5$ mTorr with $T_s = 300$ °C, $J_i/J_{Ti} \sim 1$, and $E_i \sim 20$ eV, the latter corresponding to the floating potential. The grain size, initially small, increases continuously with film thickness while the
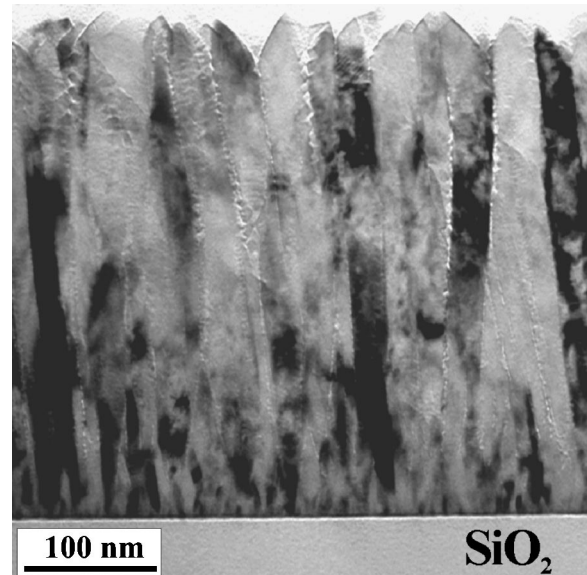

FIG. 9. Bright-field XTEM micrograph from a TiN film deposited on amorphous SiO_2 at 300 °C with a total pressure $P_t = 5$ mTorr. The ion-to-Ti flux ratio J_i/J_{Ti} incident at the growing film was ~1 with an ion energy $E_i = 20$ eV.

column boundaries become increasingly more open. The self-organized Zone T columnar microstructure forms through random nucleation, limited coarsening during coalescence, and competitive column growth. The microstructure is consistent with the one predicted by the kMC simulation in Fig. 4. The column tops are faceted due to kinetic roughening, which in combination with atomic shadowing results in deep cusps between columns and open column boundaries. The individual columns, however, are dense indicating sufficient adatom surface mobility to sustain local crystal growth. Sputtered atom energy contributes to local epitaxy.

A combination of x-ray diffraction, electron diffraction, and lattice resolution TEM imaging was employed to investigate TiN texture evolution under low-ion flux, low-energy deposition conditions ($J_i/J_{Ti} \sim 1$ and $E_i \sim 20$ eV).[74] While 111 and 002 grains, approximately 50% each by area, coexist during the early stages of film growth, the 111 grains gradually overgrow the 002 oriented grains until at thicknesses >150 nm, the film has a nearly complete 111 texture. Results consistent with those described for TiN, in which the higher-surface-energy 111 grains emerge under low-temperature, low-ion-irradiation deposition conditions, have been reported for experiments with B1–NaCl-structure $Ti_{0.5}Al_{0.5}N$,[75] ScN,[76] TaN[77] as well as for kMC simulations of fcc film growth [see Fig. 4].[78] In each of these cases, the results can be explained as being due to anisotropies in surface diffusivities and adatom potential energies as discussed in Sec. II.

For the growth of TM nitrides by reactive sputter deposition, the interplay and competition among several interrelated surface reaction and diffusional processes determine film growth kinetics, surface morphology, film microstructure, and texture.[79] The rate-limiting step for TM nitride film growth is cation incorporation which, in the above experiments, proceeds at a rate of several ML s^{-1}. The N_2 supply rate is much larger, $\lesssim 10^3$ ML s^{-1}. If N_2 molecules reach Ti adatoms not yet incorporated in the lattice, they undergo dissociative chemisorption. However, all other incident N_2 molecules are only physisorbed and desorb at kinetic rates with estimated lifetimes $\lesssim 10^{-9}$ s. This results in (001) surfaces which exhibit an essentially bulk-terminated structure with equal cation and anion number densities while 111 surfaces are fully N terminated.[79] Ti adatoms form one N back bond on (001) surfaces and three N back bonds on (111) surfaces. Thus, cation diffusivities and potential energies are higher on 001-oriented grains than on 111 grains and, following the arguments given above, Ti adatoms have a larger chance of becoming trapped at 111 sites. Consequently, 111 grains slowly and inexorably expand at the expense of the 002 grains under low-T_s, low-ion-flux growth conditions.

B. Effects of increasing E_i with $J_i/J_{Me} \lesssim 1$

Increasing the ion energy, while maintaining $J_i/J_{Me} \lesssim 1$, affects the film microstructure, primarily through linear cascade effects. Figure 10 is an XTEM image of the middle portion of a TiN film, deposited at a temperature and pressure ($T_s = 300$ °C, $P_t = 5.6$ mTorr) similar to that of the
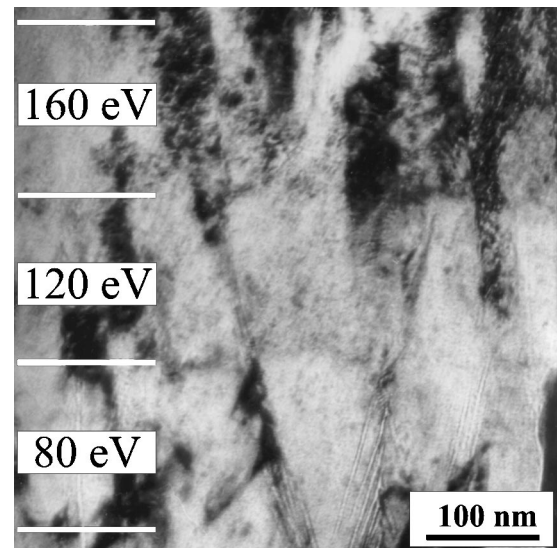

FIG. 10. Bright-field XTEM micrograph obtained from the middle portion of a 3.5-μm-thick TiN layer grown by reactive magnetron sputter deposition on steel at 300 °C with a total pressure $P_t = 5.6$ mTorr. The ion-to-Ti flux ratio J_i/J_{Ti} incident at the growing film was <1 while the ion energy E_i was varied in steps of 40 eV from 400 to 0 to 400 eV.

sample shown in Fig. 9. During the growth of the film in Fig. 10, E_i was varied in steps of 40 eV with $J_i/J_{Ti} \leqslant 1$.[80] The microstructure of $E_i \leqslant 80$ eV layers consists of dense columns with open column boundaries. As the ion energy is increased to 120 eV, the voids along column boundaries disappear and the film becomes fully dense. This is accompanied, however, by incorporation of intragranular residual damage (manifested in Fig. 10 as a darker average contrast in the $E_i = 120$ eV sublayer) whose concentration increases at higher voltages (even darker contrast in the $E_i = 160$ eV sublayer). When the energy is increased above 160–200 eV, the defect density becomes so large that local epitaxial growth on individual columns is disrupted and renucleation occurs. Figure 11, from the bottom portion of the film in Fig. 10, shows high-energy ($E_i = 200 – 400$ eV) ion-irradiation-induced densification together with a highly defective, equiaxed microstructure which forms through renucleation. The microstructure is similar to the one described in Sec. III, in which a tissue phase forms due to segregation of a reactive component. The common feature in both cases is that local crystal growth on individual columns is disrupted by repeated nucleation events.

The densification obtained in this regime ($E_i > 100$ eV) comes at a steep price, however; the high ion energy results in correspondingly high defect densities, high compressive stresses,[81–83] and inert gas incorporation.[84] Ar concentrations C_{Ar} in TiN layers deposited on amorphous SiO_2 at 350 °C as a function of E_i, between 0 and 1800 eV, with $J_i/J_{Ti} \leqslant 1$, are presented in Ref. 84. C_{Ar} is below 0.5 at. % with E_i <100 eV, while at higher ion energies C_{Ar} increases approximately linearly from 1 at. % at 200 eV to 5.5 at. % at 1800 eV.

Concurrent with the above results, x-ray and electron diffraction patterns reveal a change in TiN preferred orientation
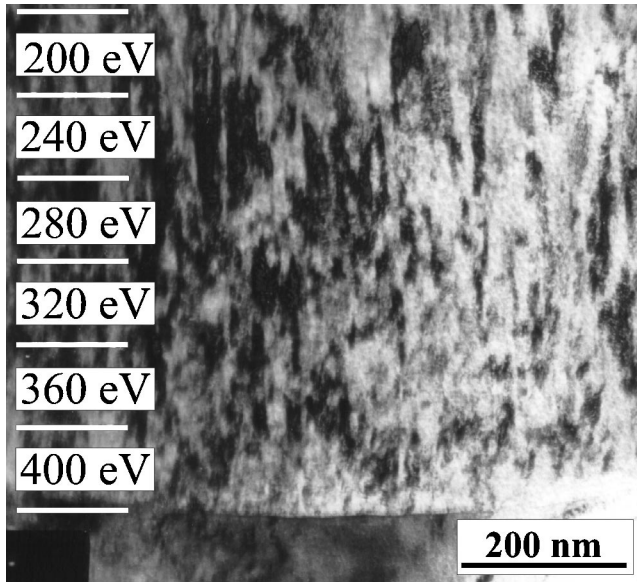
FIG. 11. Bright-field XTEM micrograph obtained from the bottom portion of the film corresponding to Fig. 10.

FIG. 12. (a) XRD ω-2θ scans from 500-nm-thick δ-TaN layers grown by reactive magnetron sputter deposition on amorphous SiO$_2$ at 350 °C as a function of J_i/J_{Ta} with $E_i = 20$ eV. (b) Normalized intensities of the (111), (002), (022), and (113) XRD peaks in (a) as a function of J_i/J_{Ta} (see Ref. 90).

from 111 to 002 with increasing E_i. However, the ion energy required to complete the transition is >800 eV, for which the films have unacceptably high stress levels. Thus, the use of high-energy, low-flux ion irradiation is not a practical approach for controlling film texture. The formation of 002 texture under such conditions is directly related to collision cascade effects.[18] Grains with open channel directions, such as 001, have higher survival probabilities due to the anisotropy of collision cascades; that is, the ion energy is distributed over larger depths in open channels leading to lower sputtering yields and less lattice distortion. Increasing the ion energy at low J_i/J_{Me} values yields only a narrow interval (100–200 eV) over which densification is obtained with acceptable levels of radiation damage and gas incorporation.

Anisotropic collisional cascades effects,[37] using ion-beam irradiation at off-normal incidence angle, have been shown to induce in-plane texture orientation in refractory metals,[85] oxides,[86] and nitrides.[87]

C. Effects of increasing J_i/J_{Me} with $E_i \lesssim 20$ eV

In this section, we discuss irradiation effects observed when the ion flux is increased while maintaining $E_i \leq 20$ eV. At such energies, which are below the threshold for bulk lattice atom displacement in TM nitrides, the residual stresses remain low, yet the effects on texture and microstructure are dramatic.

Using independent control[88] of the energy and flux of ions incident at the growing film, it has been demonstrated that the reaction paths associated with independently varying E_i and J_i/J_{Me} are quite different, even when the average kinetic energy deposited per atom $\langle E_{Me} \rangle = E_i(J_i/J_{Me})$, is maintained constant.[75] In fact, varying J_i/J_{Me} over a wide range, with $E_i \approx 20$ eV, during magnetron sputter deposition has been shown to be an effective method for controlling the microstructural evolution of polycrystalline NaCl-structure
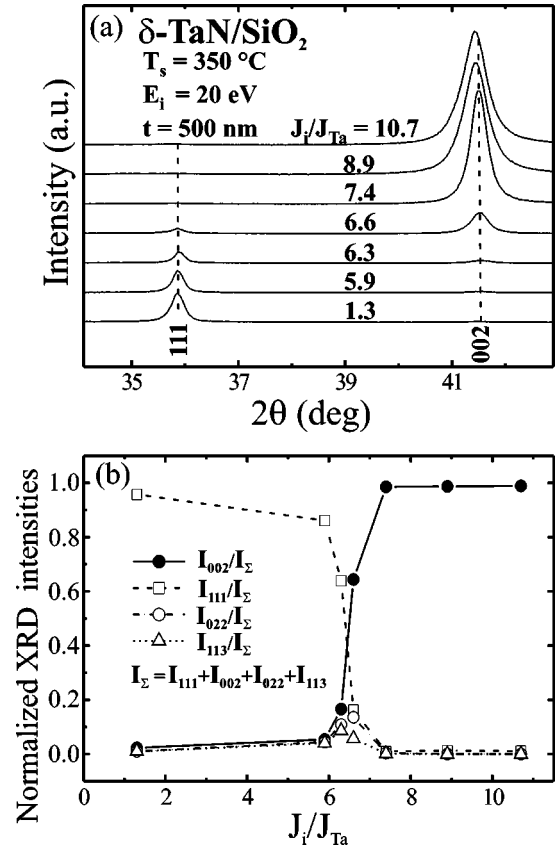
Ti$_{0.5}$Al$_{0.5}$N,[75] TiN,[74] ScN,[76] and δ-TaN,[77] while introducing negligible concentrations of residual ion-induced defects and residual stress. In these studies, Ar/N$_2$ sputtering gas mixtures with N$_2$ exceeding 10% were used, resulting in N$_2^+$ fractions in the ion flux incident at the growing films of >0.05. We use TaN deposition[77] as an example to illustrate the primary observations.

The ω-2θ and glancing-angle x-ray diffraction (XRD) scans from 500-nm-thick TaN layers grown at $T_s = 350$ °C with $E_i = 20$ eV and J_i/J_{Ta} values ranging from 1.3 to 10.7 contain predominantly (111) and/or (002) δ-TaN reflections (no other phases were detected). Typical ω-2θ results are shown in Fig. 12(a). Films grown with high flux ratios ($J_i/J_{Ta} \geq 7.4$) exhibit a complete 002 texture while those grown with $J_i/J_{Ta} < 6.3$ have a strong 111 preferred orientation with a small volume fraction of 002, 022, and 113 grains. XRD pole figures reveal, in addition, that all diffraction peak maxima are aligned along the growth direction and that peak intensities are azimuthally symmetric. The measured residual stresses are low, ranging from tensile, +1.4 GPa, in 111-textured layers (low J_i/J_{Ta} values) to slightly compressive, −0.7 GPa, in 002-oriented films (high J_i/J_{Ta} values).

The above results clearly demonstrate that the incident

ion-to-metal flux ratio can be used to selectively and controllably vary the preferred orientation of TM films from predominately 111 to 002. This is illustrated in Fig. 12(b) by plotting normalized hkl XRD peak intensities ($I_{hkl}/[I_{111} + I_{002} + I_{022} + I_{113}]$) as a function of J_i/J_{Ta}.

While XTEM images from the above-described 111-textured samples reveal an underdense Zone T microstructure similar to the one presented above in Fig. 9, results for 002 δ-TaN samples are very different. Figure 13(a) is a bright-field XTEM micrograph from a film grown with $J_i/J_{Ta} = 10$. The microstructure is still columnar, but in this case fully dense in agreement with plan-view TEM results and film density measurements.[77] The surface is also much smoother than 111-textured layers. The inset in Fig. 13(a) is a selected area electron diffraction (SAED) pattern exhibiting strong 002 and weak 111 reflections along the growth direction. The dark field images in Figs. 13(b) and 13(c), obtained using the circled portions of the 002 and 111 SAED ring segments along the film growth direction, show that microstructure evolution in δ-TaN layers grown with high J_i/J_{Ta} values also involves competitive growth. Both 002 and 111 grains are present at film thicknesses up to >200 nm. In this case, however, it is the 002 columns which win by overgrowing the 111 columns.

The above behavior can be understood based upon arguments, presented in Sec. II, regarding competitive growth between grains exposing low- versus high-diffusivity planes to the growth front with the high-flux ion irradiation switching the balance between 111 and 002 orientations. Incident 20 eV N_2^+ ions are collisionally dissociated and provide a continuous source of atomic N which can chemisorb on 001 grains ([001] is a nonpolar direction in the NaCl structure), but not on N-terminated 111 grains. This is in contrast to incident thermal N_2 species which, as discussed above, have very short lifetimes on both surfaces in the absence of a local population of free cations. Thus, increasing J_i/J_{Ta} corresponds to raising the steady-state N coverage θ_N on 001 grains while θ_N remains at a constant N-terminated value on 111 grains. This has the important consequence of decreasing cation mean free paths on (001) surfaces due to capture by N adatoms to form TaN_i ($i = 1-4$) admolecules which are more strongly bonded to the surface than Ta adatoms, and therefore have lower surface mobilities. That is, in the presence of an atomic N source, the effective 001 adatom potential energy decreases below that on the 111. Consequently, the net flux of cations from 002 to 111 oriented grains is reversed under high-flux conditions, resulting in the development of 002 texture.

In addition to controllably switching the texture from 111 to 002 with increasing ion flux, there is a corresponding increase in layer density and a decrease in surface roughness from underdense δ-TaN layers with intercolumnar voids and self-organized growth mounds separated by deep surface trenches[89] to fully dense layers with smoother surfaces. The densification is attributed to less pronounced kinetic roughing due to ion-irradiation enhanced surface mobilities resulting in smoother surfaces with less atomic shadowing.
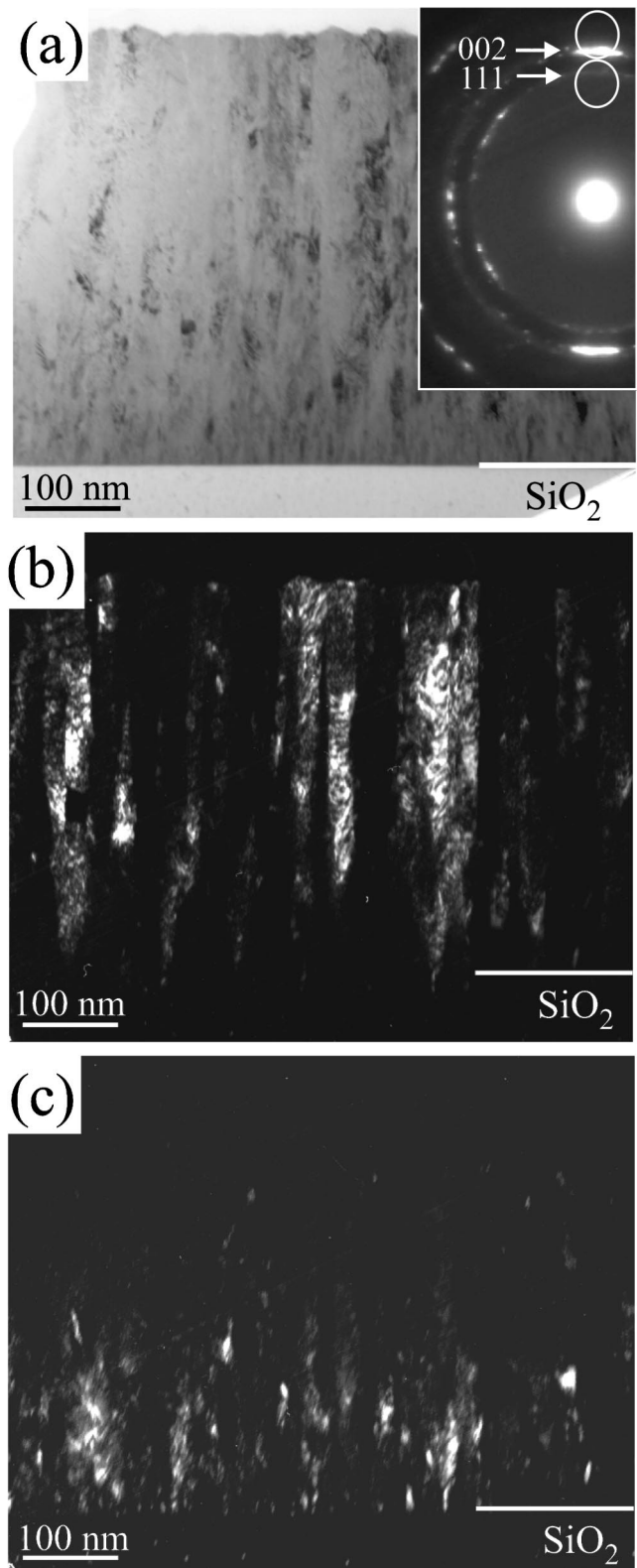

FIG. 13. (a) Bright-field XTEM micrograph and corresponding SAED pattern obtained from a δ-TaN layer grown by reactive magnetron sputter deposition on amorphous SiO_2 at 350 °C with $E_i = 20$ eV and $J_i/J_{Ta} = 10.7$; (b) and (c) are dark field XTEM micrographs imaged using 002 and 111 diffraction rings indicated by circles in the SAED pattern in (a) (see Ref. 90).

Increasing the ion flux from 1 to 10 with $E_i \sim 20$ eV results in a transition from underdense 111 to a dense 002 texture. In both cases, however, competitive texture evolution follows random nucleation on the amorphous substrate. It is possible, however, to use texture inheritance[37] to select the preferred orientation during the nucleation stage. This concept was utilized to achieve dense, highly 111-oriented TM nitride (TiN[90] and TaN[91]) films. Ti underlayers 25 nm thick were first deposited on amorphous substrates at 80 °C with $J_i/J_{Me} = 2$ and $E_i = 11$ eV. The layers are fully dense with a Zone II structure consisting of cylindrical grains having very strong 0002 orientation. The TM nitride overlayers were then deposited with high J_i/J_{Me} values (>10) and $E_i \sim 20$ eV, which on bare amorphous substrates result in dense 002 layers. In this case, however, local epitaxy on 0002 Ti grains results in fully dense TM nitride layers with a strong 111 texture and competitive grain growth is completely eliminated.

V. SUMMARY AND FUTURE DIRECTIONS

The atomic-scale understanding of microstructural evolution, necessary for the controlled manipulation of the properties of thin film systems, is growing rapidly. However, we are still far from having an accurate quantitative description. A concerted program, with the ultimate goal being the ability to design, at the atomic scale, new materials and new structures having a particular desired set of properties, might include the following components.

(1) Detailed experimental measurements, for simple model systems, of orientation-dependent adatom transport parameters (activation barriers for surface diffusion, island edge diffusion, step edge attachment/detachment, step edge Ehrlich barriers, and adatom formation energies) and orientation-dependent step and kink formation energies. These measurements should be carried out on well-defined single crystal surfaces as has recently been done by Kodambaka *et al.*[92] for TiN.

(2) The above kinetic and thermodynamic parameters should then be incorporated into multiscale (in both time and space) models of the early stages of microstructure development including island growth and coalescence. The structural evolution models will be based upon combinations of, for example, density functional theory calculations, molecular dynamics simulations, kinetic Monte Carlo simulations, and continuum methods with accurate atomistically derived information driving each successive scale in the modeling. The most difficult part is always the transition to the continuum. However, the recent introduction of level set methods[93] allows the input of atomistic information into a continuum description of in-plane film growth while preserving the discreteness of each atomic layer and dealing with local singularities in a natural manner.[48]

(3) Model predictions must be verified by complementary *in situ* studies of film-growth dynamics utilizing, for example, scanning tunneling microscopy, low-energy electron microscopy, and TEM. The experimental results should be compared to model predictions and, if necessary, fed back

into a further round of model refinement. Recent advances in the development of aberration-corrected electron microscopes[94] render these new-generation instruments much more suitable for such experiments. They provide larger working volumes between the pole pieces for carrying out *in situ* film growth while maintaining atomic resolution imaging and providing ultrafast recording.

(4) The next stage is to extend both experiments and modeling/simulation to include coarsening during coalescence, competitive grain growth, and texture evolution. This will require the addition of orientation-dependent grain boundary energies into the models and accounting for the role of strain in both experiments and models.[95]

(5) A further extension is to include postdeposition aging and annealing to describe the thermal stability of the as-deposited microstructural features to recrystallization and abnormal grain growth, metastable multi-component[96] thin film systems, and self-organized nanostructures (e.g., nanolamellae, nanocolumns, etc.).

While portions of each of these tasks are being carried out at different laboratories around the world on a variety of materials systems, it will likely require a focused effort by several laboratories working collaboratively to achieve the above goal.

ACKNOWLEDGMENTS

[1] B. A. Movchan and A. V. Demchishin, Fiz. Met. Metalloved. **28**, 83 (1969).
[2] J. V. Sanders, in *Chemisorption and Reactions on Metallic Films*, edited by J. R. Anderson (Academic, London, 1971), p. 1.
[3] J. A. Thornton, Annu. Rev. Mater. Sci. **7**, 239 (1977).
[4] R. Messier, A. P. Giri, and A. R. Roy, J. Vac. Sci. Technol. A **2**, 500 (1984).
[5] C. R. M. Grovenor, H. T. G. Hentzell, and D. A. Smith, Acta Metall. **32**, 773 (1984).
[6] D. A. Smith and A. Ibrahim, Mater. Res. Soc. Symp. Proc. **317**, 401 (1994).
[7] R. A. Roy and R. Messier, Mater. Res. Soc. Symp. Proc. **38**, 363 (1985).
[8] J. A. Thornton, J. Vac. Sci. Technol. A **4**, 3059 (1986).
[9] P. B. Barna and M. Adamik, Thin Solid Films **317**, 27 (1998).
[10] E. Bauer, "Fiber Texture," in *The Ninth National Vacuum Symposium of the American Vacuum Society*, edited by George H. Bancroft (Macmillan, New York, 1963), p. 35.
[11] M.H. Fracombe, in *Basic Problems in Thin Film Physics, Proc. Intern. Symp. Clausthal-Goettengen 1965*, edited by R. Niedermayer and H. Mayer (Vandenhoeck & Ruprecht, Goetingen, 1966), p. 35.
[12] K. L. Chopra, *Thin Film Phenomena* (McGraw–Hill, New York, 1969).
[13] J. A. Thornton, J. Vac. Sci. Technol. **11**, 666 (1974).
[14] D. J. Hendersson, M. H. Brodsky, and P. Chaudhari, Appl. Phys. Lett. **25**, 641 (1974).

[15]A. G. Dirks and H. J. Leamy, Thin Solid Films **47**, 219 (1977).

[16]D. W. Hoffman and J. A. Thornton, Thin Solid Films **45**, 387 (1977).

[17]B. Lewis and J. C. Anderson, *Nucleation and Growth of Thin Films* (Academic, New York, 1978).

[18]D. Dobrev, Thin Solid Films **92**, 41 (1982).

[19]K.-H. Müller, J. Appl. Phys. **58**, 2573 (1985).

[20]J. M. E. Harper, J. J. Cuomo, and H. T. G. Hentzell, J. Appl. Phys. **58**, 550 (1985).

[21]H. J. Leamy, G. H. Gilmer, and A. G. Dirks, in *Current Topics in Materials Science*, edited by E. Kaldis (North-Holland, Amsterdam, 1980), Vol. 6.

[22]D. J. Srolovitz, J. Vac. Sci. Technol. A **4**, 2925 (1986).

[23]S. Lichter and J. Chen, Phys. Rev. Lett. **56**, 1396 (1986).

[24]K.-H. Müller, Phys. Rev. B **35**, 7906 (1987).

[25]E. Kay, F. Parmigiani, and W. Parrish, J. Vac. Sci. Technol. A **6**, 3074 (1988).

[26]K. Kobashi, K. Nishimura, Y. Kawate, and T. Horiuchi, Phys. Rev. B **38**, 4067 (1988).

[27]A. R. Badzian and R. C. De Vries, Mater. Res. Bull. **23**, 385 (1988).

[28]T. Hashimoto, K. Okamoto, K. Hara, M. Kamiya, and M. Fujiwara, Thin Solid Films **182**, 197 (1989).

[29]J. Musil, S. Kadlec, V. Valvoda, R. Kuzel, and R. Cerny, Surf. Coat. Technol. **43/44**, 259 (1990).

[30]W. A. Yarbrough and R. Messier, Science **247**, 688 (1990).

[31]D. A. Smith, in *Materials Interfaces, Atomic Level Structure and Properties*, edited by D. Wolf and S. Yip (Chapman and Hall, London, 1992), Chap. 6.

[32]D. A. Smith and A. Ibrahim, Mater. Res. Soc. Symp. Proc. **317**, 401 (1994).

[33]M. Kotrla, J. Krug, and P. Smilauer, Phys. Rev. B **62**, 2899 (2000).

[34]J. A. Vanables, *Introduction to Surface and Thin Film Processes* (Cambridge University Press, Cambridge, 2000).

[35]C. V. Thompson, Annu. Rev. Mater. Sci. **20**, 245 (1990).

[36]C. V. Thompson and R. Carel, Mater. Sci. Eng., B **32**, 211 (1995).

[37]J. M. E. Harper and K. P. Rodbell, J. Vac. Sci. Technol. B **15**, 763 (1997).

[38]R. Winand, Electrochim. Acta **39**, 1091 (1994); D. Landolt, J. Electrochem. Soc. **149**, S9 (2002).

[39]C. Ratsch and Venables in this volume.

[40]D. Cahill in this volume.

[41]D. W. Paschley, Philos. Mag. **15**, 173 (1966); H. Lewis, Thin Solid Films **7**, 179 (1971).

[42]J. F. Pocza, A. Barna, and P. B. Barna, J. Vac. Sci. Technol. **6**, 172 (1969); J. F. Pocza, A. Barna, P. B. Barna, I. Pozsgai, and G. Radnoczi, Jpn. J. Appl. Phys. **2**, 525 (1974).

[43]M. Zhang, M. Yu. Efremov, F. Schiettekatte, E. A. Olson, A. T. Kwan, S. L. Lai, T. Wiskder, J. E. Greene, and L. H. Allen, Phys. Rev. B **62**, 10458 (2000), and references therein.

[44]D. W. Pashley, in *Epitaxial Growth*, edited by J. W. Matthews (Academic, New York, 1975), Part B, p. 1; J. F. Pocza, A. Barna, and P. B. Barna, Krist. Tech. **5**, 315 (1970); G. Honjo and K. Yagi, in *Current Topics in Materials Science*, edited by E. Kaldis (North-Holland, Amsterdam, 1975), Vol. 6, p. 195.

[45]J. F. Pocza, in *Proceedings of the Second Colloquium on Thin Films*, edited by E. Hahn (Hungarian Academy of Sciences, Budapest, 1967), p. 93.

[46]D. Henderson, M. H. Brodsky, and P. Chaudhari, Appl. Phys. Lett. **25**, 64 (1974).

[47]R. Messier, J. Vac. Sci. Technol. A **4**, 490 (1986), and references therein.

[48]F. H. Baumann, D. L. Chopp, T. Díaz de la Rubia, G. H. Gilmer, J. E. Greene, H. Huang, S. Kodambaka, P. O'Sullivan, I. Petrov, MRS Bull. **26**, 182 (2001); G. H. Gilmer, H. Huang, T. Diaz de la Rubia, J. Dalla Torre, and F. Baumann, Thin Solid Films **365**, 189 (2000).

[49]J. M. Schneider, K. Larsson, J. Lu, E. Olsson, and B. Hjörvarsson, Appl. Phys. Lett. **80**, 1144 (2002).

[50]P. B. Barna, in *Proceedings of the Ninth International Vacuum Congress*, Madrid, Spain 1983, p. 382, and references therein (unpublished).

[51]A. Csanady, Y. Pitton, H. J. Mathieu, K. Kessler, R. Fuchs, and M. Textor, Surf. Interface Anal. **21**, 546 (1994).

[52]R. Michel, J. Castaldi, C. Allasia, C. Jourdan, and J. Derrien, Surf. Sci. **95**, 309 (1980), and references therein.

[53]P. B. Barna, M. Adamik, G. Safran, B. Pecz, A. Bergauer, and H. Bangert, Phys. Status Solidi A **146**, 31 (1994), and references therein.

[54]S. Veprek, J. Vac. Sci. Technol. A **17**, 2401 (1999).

[55]T. Zehnder and J. Patscheider, Surf. Coat. Technol. **133,134**, 138 (2000).

[56]P. H. Mayrhofer and C. Mitterer, Surf. Coat. Technol. **133,134**, 131 (2000).

[57]J. Musil, H. Hrubý, P. Zeman, H. Zeman, R. Cerstvý, P. H. Mayrhofer, and C. Mitterer, Surf. Coat. Technol. **142–144**, 603 (2001).

[58]A. A. Voevodin, J. J. Hu, T. A. Fitz, and J. S. Zabinski, Surf. Coat. Technol. **146,147**, 351 (2001).

[59]P. B. Barna, M. Adamik, U. Kaiser, S. Laux, H. Bangert, M. Pulliainen, and K. A. Pishow, Surf. Coat. Technol. **100,101**, 72 (1998).

[60]P. B. Barna, M. Adamik, L. Labar, L. Kover, J. Toth, A. Devenyi, and R. Manaila, Surf. Coat. Technol. **125**, 147 (2000).

[61]C. A. Neugebauer, Thin Solid Films **6**, 443 (1970); A. F. Jankowski, *ibid.* **332**, 272 (1998).

[62]J. E. Sundeen and R. C. Buchanan, Sens. Actuators A **90**, 118 (2001).

[63]Q.-C. Zhang, Sol. Energy Mater. Sol. Cells **62**, 63 (2000).

[64]K. Bewilogua, C. V. Cooper, C. Specht, J. Schröder, R. Wittorf, and M. Grischke, Surf. Coat. Technol. **132**, 275 (2000).

[65]J. S. Zabinski, M. S. Donley, V. J. Dyhouse, and N. T. McDevit, Thin Solid Films **214**, 156 (1992); A. A. Voevodin and J. S. Zabinski, *ibid.* **370**, 223 (200).

[66]J. M. Schneider, W. D. Sproul, and A. Matthews, Surf. Coat. Technol. **98**, 1473 (1998).

[67]A. Kovacs, P. B. Barna, and J. L. Labar, Thin Solid Films **433**, 78 (2003).

[68]A. Barna, P. B. Barna, G. Radnoczi, F. M. Reicha, and L. Toth, Phys. Status Solidi A **55**, 427 (1979).

[69]C. Eisenmenger-Sittner, H. Bangert, H. Stori, J. Brenner, and P. B. Barna, Surf. Sci. **489**, 161 (2001).

[70]J. E. Greene, S. A. Barnett, J.-E. Sundgren, and A. Rockett, in *Ion Beam Assisted Film Growth*, edited by T. Itoh (Elsevier, Amsterdam, 1988), Chap. 5.

[71]I. Petrov, A. Myers, J. E. Greene, and J. R. Abelson, J. Vac. Sci. Technol. A **12**, 2846 (1994).

[72]L. Hultman, W.-D. Münz, J. Musil, S. Kadlec, I. Petrov, and J. E. Greene, J. Vac. Sci. Technol. A **9**, 434 (1991).

[73]W. D. Westwood, J. Vac. Sci. Technol. A **15**, 1 (1978).

[74]L. Hultman, J.-E. Sundgren, J. E. Greene, D. B. Bergstrom, and I. Petrov, J. Appl. Phys. **78**, 5395 (1995).

[75]I. Petrov, F. Adibi, J. E. Greene, L. Hultman, and J.-E. Sundgren, Appl. Phys. Lett. **63**, 36 (1993); F. Adibi, I. Petrov, J. E. Greene, L. Hultman, and J.-E. Sundgren, J. Appl. Phys. **73**, 8580 (1993).

[76]D. Gall, I. Petrov, N. Hellgren, L. Hultman, J.-E. Sundgren, and J. E. Greene, J. Appl. Phys. **84**, 6034 (1998).

[77]C.-S. Shin, D. Gall, Y.-W. Kim, N. Hellgren, I. Petrov, and J. E. Greene, J. Appl. Phys. **92**, 5084 (2002).

[78]The low-surface energy, high-diffusivity surfaces in fcc and B1–NaCl structure are {111} and {100}, respectively.

[79]D. Gall, S. Kodambaka, M. A. Wall, I. Petrov, and J. E. Greene, J. Appl. Phys. **93**, 9086 (2003).

[80]I. Petrov, L. Hultman, U. Helmersson, J.-E. Sundgren, and J. E. Greene, Thin Solid Films **169**, 299 (1989).

[81]H. Windishman, J. Appl. Phys. **62**, 1800 (1987).

[82]J. A. Thornton and D. W. Hoffman, Thin Solid Films **171**, 5 (1989).

[83]C. A. Davis, Thin Solid Films **226**, 30 (1993).

[84]I. Petrov, L. Hultman, J.-E. Sundgren, and J. E. Greene, J. Vac. Sci. Technol. A **10**, 265 (1992).

[85]L. S. Yu, J. M. E. Harper, J. J. Cuomo, and D. A. Smith, J. Vac. Sci. Technol. A **4**, 443 (1986).

[86]R. M. Bradley, J. M. E. Harper, and D. A. Smith, J. Appl. Phys. **60**, 4160 (1986).

[87]C.-H. Ma, Ph.D. thesis, University of Illinois.

[88]I. Petrov, F. Adibi, J. E. Greene, W. D. Sproul, and W.-D. Münz, J. Vac. Sci. Technol. A **10**, 3283 (1992).

[89]L. Hultman, L. R. Wallenberg, M. Shinn, and S. A. Barnett, J. Vac. Sci. Technol. A **10**, 1618 (1992).

[90]J.-S. Chun, I. Petrov, and J. E. Greene, J. Appl. Phys. **86**, 3633 (1999).

[91]C.-S. Shin, I. Petrov, and J. E. Greene (unpublished).

[92]S. Kodambaka, S. V. Khare, V. Petrova, A. Vailionis, I. Petrov, and J. E. Greene, Surf. Sci. **513**, 468 (2002); S. Kodambaka, S. V. Khare, V. Petrova, D. D. Johnson, I. Petrov, and J. E. Greene, Phys. Rev. B **67**, 035409 (2003); S. Kodambaka, V. Petrova, S. V. Khare, A. Rockett, I. Petrov, and J. E. Greene, Phys. Rev. Lett. **89**, 176102 (2002); S. Kodambaka, V. Petrova, A. Vailionis, I. Petrov, and J. E. Greene, Surf. Sci. **526**, 85 (2003).

[93]J. A. Sethian, *Level Set Methods and Fast Marching Methods* (Cambridge University Press, Cambridge, 1999).

[94]See, e.g., http://cmm.mrl.uiuc.edu/CMM-TEAM.html and the links therein.

[95]J. A. Floro, E. Chason, R. C. Cammarata, and D. J. Srolovitz, MRS Bull. **27**, 19 (2002).

[96]See, e.g., A. Hörling, L. Hultman, M. Odén, J. Sjölén, and L. Karlsson, J. Vac. Sci. Technol. A **20**, 1815 (2002).